

Large-Area Material and Junction Damage in c-Si Solar Cells by Potential-Induced Degradation

Chuanxiao Xiao,* Chun-Sheng Jiang,* Steve P. Harvey, Dana Sulas, Xihan Chen, Jun Liu, Jie Pan, Helio Moutinho, Andrew Norman, Peter Hacke, Steve Johnston, and Mowafak Al-Jassim

This paper reports a new potential-induced degradation (PID) mechanism for crystalline silicon (c-Si), where Na diffuses everywhere and causes large-area material and junction degradation with point defects. Multiple characterization techniques are combined—Kelvin probe force microscopy, electron-beam induced current, dark lock-in thermography, transmission electron microscopy, time-of-flight secondary-ion mass spectrometry, and microwave photo-conductance decay—as well as density functional theory (DFT) calculations. These characterization techniques and theoretical calculations are complementary in various aspects of a material's chemical, structural, electrical, and optoelectrical nature, as well as in atomic, nanometer, micrometer, millimeter, and cell and module scales. All results point consistently to a new discovery: substantial large-area deterioration of materials and junctions play a major role in c-Si PID (in addition to the previously reported local shunting defect caused by Na diffusion to planar defects). This new finding reveals a key PID component and leads to a new strategy for tailoring c-Si photovoltaics to ultimately resolve the PID issue.

1. Introduction

Crystalline silicon (c-Si) solar modules are one of the most important renewable energy technologies, comprising more than 80% of the photovoltaic (PV) market share and being deployed at large scale approaching 100 gigawatts annually. Potential-induced degradation (PID) is an important degradation component in all types of major solar modules, often causing massive decreases in module performance.^[1–5] PID is due to the potential difference between the module frame/glass and solar cell, and the degradation becomes more severe with increased system voltage of a solar array. For c-Si-based modules, PID has been widely reported to be related to sodium-decorated extended defects that exist in the Si p-n junction, causing local electrical shunting.^[6–14] However, it is unclear whether extended defects such as stacking faults exist

before PID and provide a fast path of Na diffusion, or whether planar defects form as a result of Na-induced stress in the Si crystal.^[12] Others have reported that a defective cell surface or built-in stress in the crystal growth process could lead to a higher possibility of PID.^[15]

PID is complicated by many different degradation kinetics and mechanisms among different types of solar modules. More importantly, it is questionable whether local shunting of Na-decorated planar defects in c-Si modules is the only major mechanism associated with massive degradation or even with module failure. Several empirical methods to prevent or minimize PID have been applied at the cell and module level, such as: increasing the refractive index of SiN_x (antireflection coating) to avoid Na accumulation,^[16–21] adding a SiO_x layer before SiN_x deposition to increase the Na diffusion barrier,^[22–24] and switching to higher bulk resistivity of

encapsulant materials to reduce the leakage current.^[25–29] These modifications can effectively slow down the degradation process, which helps modules pass the International Electrotechnical Commission (IEC) 62804 standard test.^[30] However, one cannot be confident that these are permanent solutions for avoiding PID. Fully eliminating PID requires a deeper understanding of the fundamental mechanisms. Today, many PV module manufacturers promote their products as “PID resistant” or “PID-free,” as they have passed the test sequences in accordance with the IEC's standards. However, the standard testing is not fully insured to accurately predict whether the solar cells or encapsulants used for module packaging are PID-eliminated in long-term for many years.^[31,32]

Furthermore, new technologies applied to modern solar panels has been growing rapidly and the new products have been installed recently, but there are no long-term records of performance and it is highly doubtful whether the modules would be resistant to PID. For example, adding a thin layer of SiO₂ between the silicon and the SiN_x coating makes the module suffered no degradation for the first 6 days even under harsher accelerate life test (ALT) conditions, however, after longer time the modules lost more than 10% of their initial power.^[24] Therefore, discovery of new PID mechanisms and more in-depth

Dr. C. Xiao, Dr. C.-S. Jiang, Dr. S. P. Harvey, Dr. D. Sulas, Dr. X. Chen, Dr. J. Liu, Dr. J. Pan, Dr. H. Moutinho, Dr. A. Norman, Dr. P. Hacke, Dr. S. Johnston, Dr. M. Al-Jassim
National Renewable Energy Laboratory, Golden
CO 80401, USA
E-mail: chuanxiao.xiao@nrel.gov; chun.sheng.jiang@nrel.gov

DOI: 10.1002/solr.201800303

understanding of the mechanisms are highly demanded for both the existing and newly-emerging c-Si PV technologies. The development of ALT conditions must be tied to understanding the physics and chemistry of all the underlying degradation mechanisms.

In this study, we report a large area (millimeter scale) of damage to the material and p-n junction by PID that occurred at the millimeter scale, rather than point shunts associated with planar defects. By characterizing the electric field in heavily PID-degraded regions with Kelvin probe force microscopy (KPFM), we found a broad change in voltage drop across the junction. More importantly, the transition between good and degraded areas is abrupt—about 1 μm . This abruptness is not consistent with the reported local junction shunting, but leads to proposing a new PID mechanism with actual large-area material and junction degradations. We further studied the degradations in various aspects of the material's chemical, structural, electrical, and optoelectrical nature by using a set of complementary characterizations as well as first-principles calculations. These results consistently elucidate a new PID mechanism—that the large-area point defects associated with Na are responsible for the c-Si solar module degradation. Our results will open a new research path to study PID and motivates the community to search approaches to ultimately eliminate PID and/or establish new ALT strategy.

2. Experimental Section

2.1. Sample Preparation

The Si solar cell studied here is a conventional **Al back-surface field (Al-BSF)** cell, with a boron-doped p-type multicrystalline Si (mc-Si) bulk, a junction formed by a phosphorous-doped emitter, and a SiN_x antireflection layer on the top. In sample preparation for the microscopic characterizations, the cell should be taken out of the module after PID stressing without changing/damaging the cell. Therefore, we developed a procedure to stress a mini-module in which a mc-Si cell was sandwiched between a glass substrate and superstrate with pre-polymerized ethylene vinyl acetate (EVA) as encapsulant. All the layer materials were held together with clamps without melting the EVA. After laboratory PID stressing, the cell was easily removed from the mini-module without mechanical damage.

We stressed the sample by applying a constant bias voltage of **−1500 V to the mini-module** (cell in short circuit) and grounding the whole glass surface by attaching an Aluminium foil, in an environmental chamber at a temperature of 25 °C and 10% relative humidity. We used this harsher stressing conditions to accelerate the PID for longer time. We then delaminated the mini-module to extract the cell. We identified pieces of the cell with heavy PID degradation using photoluminescence (PL) imaging (dark PL area), and we cut out these pieces for the various microscopic characterizations. Because different characterizations require different sample configuration and preparation procedures, the samples for different techniques are not compatible, i.e., it was not able to measure on the same area with the different characterization techniques. Instead, we select the most degraded areas with similar degradation degrees as identified by PL imaging, and cut out to separated pieces for the different characterizations.

For KPFM imaging on cross section of the solar cell, we break the sample across the darkest PL area and used silver epoxy to glue the cell emitter (n^+) face to another piece of silicon. This sandwich sample preparation prevents probe drop-off when scanning the probe close to the front side of the cell or across the junction. We chemical-mechanically polished the cell with deionized water using a set of diamond pads of 30 μm , 9 μm , 3 μm , 1 μm , 0.5 μm , 0.1 μm ; then polished the cross section with silica colloids suspension (0.05 μm) using a soft cloth for 1 min.

For in situ KPFM studies to monitor evolution of the junction potential, we encapsulated a small piece of mc-Si cell ($\approx 0.5 \times 0.8 \text{ cm}^2$) to make an identical structure to a real solar module (with EVA melted). The working solar cell (shunt resistance larger than 500 $\Omega\text{-cm}^2$) was partially covered by a glass piece and partially exposed on the cell's front contact so that a bias voltage can be applied across the cell, as needed for KPFM measurements. We then polished the sample with the same procedure to make an adequately flat cross-sectional surface. To partially recover the PID, we heated the sample on a hot plate at 300 °C for 30 min.

2.2. Kelvin Probe Force Microscopy

KPFM is based on the noncontact mode of an atomic force microscope (Veeco D5000 and Nanoscope V). KPFM measures electrostatic potential on the sample surface with a spatial resolution of $\approx 30 \text{ nm}$ and a potential resolution of $\approx 10 \text{ mV}$.^[33] Topographic and electrical images were collected simultaneously during the probe scanning. To avoid the effect of surface charges, we applied a bias voltage to a working device and measured the corresponding changes of surface potential on the cross section. Because the surface-charge configuration should not change with a small bias voltage (V_b) of 0–2 V, the measured change of the cross-section surface potential is about the same as the potential change in the bulk. In this way, we determined the potential change in the bulk by measuring the surface potential change across the p-n junction.^[34] Fresh, degraded, and heat-treated samples were examined by KPFM. In situ KPFM^[35] monitors the evolution of potential across the p-n junction for a long period of PID-stressing time (≈ 40 days) at room temperature.

2.3. Photoluminescence and Dark Lock-In Thermography

PL images are recorded using a cooled (−50 °C) Princeton Instruments PIXIS 1024BR charge-coupled device (CCD) camera with an InP wafer as a long-pass filter. The samples are photoexcited using an array of continuous wave (CW) 808-nm laser diodes equipped with diffusers. Dark lock-in thermography (DLIT) images are collected with a Cedip Silver 660 M (FLIR SC5600-M) InSb camera using lock-in data acquisition. Heating is generated using a −1 V reverse-bias current pulsed at a frequency of 100 Hz.

2.4. Microwave Photoconductance Decay

Time-resolved microwave photoconductivity is measured by photoexciting the cell with a nanosecond 500-nm laser pulse and

recording the change in reflectivity of a 20-GHz microwave coupled to the sample surface through a waveguide. The signals at various time delays are recorded using an oscilloscope triggered by the laser. Laser pulses at 500 nm are generated from a Continuum Panther optical parametric oscillator pumped with a Continuum Powerlite Q-switched Nd:YAG laser at 355 nm.

2.5. Electron-Beam Induced Current and Electron Back-Scattered Diffraction

EBIC was performed by using an FEI Nova630 field-emission scanning electron microscope (SEM) using a Matelect current amplifier, operating at 5-kV, 0.9-nA beam condition. Electron back-scattered diffraction (EBSD) uses the FEI SEM equipped with an EDAX Hikari camera; the electron beam condition is 20 kV, 1.4 nA.

2.6. Time-of-Flight Secondary-Ion Mass Spectrometry

A TOF-SIMS spectrometer (ION-TOF TOF-SIMS V) was used to image lateral Na distribution and measure depth profile on the plane-view sample. The vertical Na distribution was also imaged on cross-sectional samples. Analysis was performed by using a 3-lens, 30-keV Bi-Mn primary ion beam scanned over a $500 \times 500 \mu\text{m}^2$ area. Three-dimensional tomography was acquired via a Bi_3^{++} ion beam cluster with 100-ns pulse width and 0.1-pA pulsed beam current, which allows a lateral resolution exceeding 100 nm in the measurement.^[36] TOF-SIMS data were acquired from both cross-sectional and plane-view samples.

2.7. Density-Functional Theory Calculation

First-principles calculations were performed with the Vienna Ab-Initio Simulation Package (VASP) using the projector-augmented-wave (PAW) potentials.^[37] We employed density functional theory (DFT) in the generalized gradient approximation^[38] and Nudged Elastic Band method (NEB) to estimate the diffusion barriers. Standard pseudopotentials are used for Na (Na_pv) and Si with a cut-off energy of 390 eV for the plane-wave basis set. A $2 \times 2 \times 2$ supercell with 64 Si atoms was constructed for defect calculations and was relaxed with $2 \times 2 \times 2$ Gamma k-point mesh. The convergence criterion is the total energy difference for each electronic step less than 10^{-5} eV, and total force exerted on each ion is less than $0.02 \text{ eV } \text{\AA}^{-1}$.

3. Experimental Results

3.1. Electrical Potential Change of the p-n Junction

PID occurs when the module's voltage and leakage current drive positive ions to migrate into the cell from the solar glass and encapsulant. Na, in particular, is believed to have a profound impact on this type of degradation, as we show in the schematic in Figure 1a. On the stressed 6×6 inches cell, we observed that the area normalized shunt resistance dropped from 6.2×10^5

$\Omega \text{ cm}^2$ to $52 \Omega \text{ cm}^2$, and that the cell was stress to the degree, where the small shunting resistance dominated the Dark I - V characteristics (Figure S1, Supporting Information). From this dark I - V curve, reliable recombination current J_{02} could not be extracted. After PID stress in stage 2 in Figure S1, Supporting Information, PL image of the cell was taken, and small pieces with heavily degraded areas (dark PL areas) were cut out for KPFM and other characterizations (Figure S2, Supporting Information). Because of the edge shunting by mechanical cutting/cleaving and the heavily-degraded region included, I - V of the small pieces had even smaller normalized shunt resistance, which dominated the dark I - V curves.

On a heavily PID-stressed Si cell piece, we investigate the electrical potential across the p-n junction on the cross section through the darkest PL area between the two silver grids over a total length of $\approx 2 \text{ mm}$ (indicated in Figure 1b). We found three significantly different kinds of areas—labeled as “No PID,” “abnormal junction area,” and “transition area,”—where the electric-field peak or the potential drop is, respectively, at the normal junction location, at the cell front surface, and between them. Typical KPFM results are shown in Figure 1c–n. In contrast to the current knowledge of PID—that is, junction shunts in highly localized spots within a few micrometers range—we observed a large, continuous PID-affected area ($\approx 1.5 \text{ mm}$) with abnormal electrical potential in the junction area. We identified the large PID-affected area with abnormal potential by random selection in every $100 \mu\text{m}$ along the whole area ($\approx 1.5 \text{ mm}$) by adequately dense sampling. We also observed normal electrical potential with no PID effect across the junction in the regions under the metal grids and nearby areas. In the areas between the normal and abnormal regions, we observed either transitional potential behavior or a mixture of normal and abnormal potentials.

Figure 1c–g show the results from the “No-PID” region. Figure 1c is an AFM of the cross section, and Figure 1d shows the corresponding potential image at a reverse bias voltage V_b of -1.5 V . The black, light purple, and light blue dashed lines from top to bottom in Figure 1c–d were drawn following the Si/Ag-epoxy interface, p-n junction location, and depletion edge of the p-type Si, respectively. Figure 1e shows the line profiles of potential averaged from the potential images and aligned with their corresponding AFM line profile. We took the potential images with varying V_b applied to the device to derive the potential change in the bulk by measuring the surface potential changes. The 0-V potential profile was subtracted from the -0.5 V and -1.5 V potential profiles (Figure 1e) to get the profiles of potential differences (Figure 1f). The V_b -induced change in the electrical field was obtained by taking the first derivative of the potential difference. The peak of the electric field indicates the p-n junction location (Figure 1g), which is $\approx 400 \text{ nm}$ from the cell surface or epoxy/cell interface, consistent with the junction depth. The junction depletion width is $\approx 500 \text{ nm}$ as estimated from the electric-field profile at -0.5 V , which is also consistent with that of a conventional industrial solar cell. Therefore, we conclude that the p-n junction in this region behaves normally from the perspective of electrical potential.

Figure 1h–j show typical KPFM results in the PID-affected region. The potential image (Figure 1i) and the electric-field peak (Figure 1j) both show a potential drop at the cell/Ag-epoxy interface. The V_b applied to the Si cell should drop at the p-n

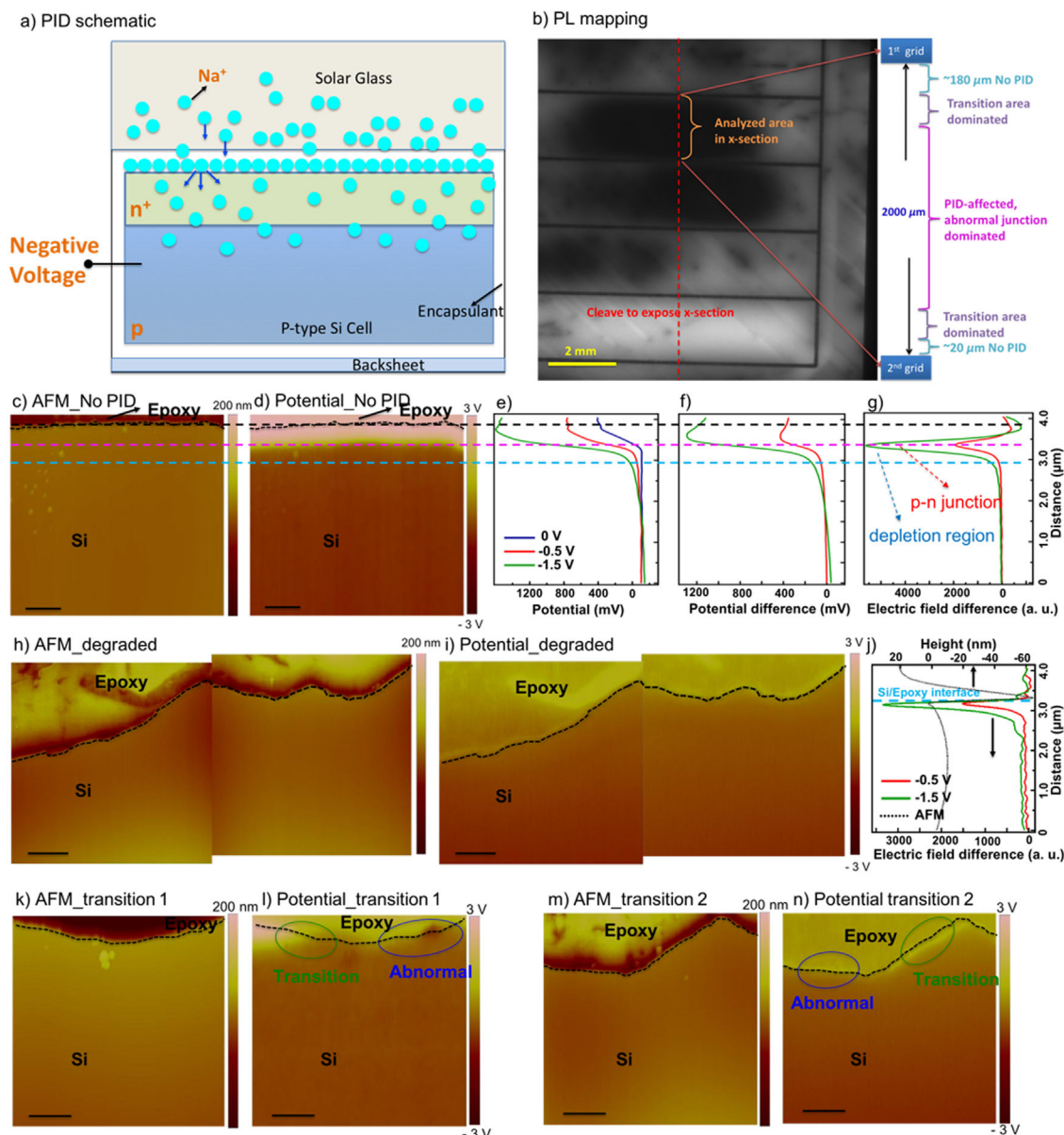


Figure 1. a) Schematic of PID; b) PL mapping and schematic illustration of analyzed area; c) AFM of a good area with normal p-n junction; d) the KPFM image at -1.5 V corresponding to c); e) potential profiles of an area in d); f) potential difference curves; g) electric-field difference curves showing a good p-n junction characteristic; h) AFM of a PID-affected area; i) the KPFM potential image at -1.5 V corresponding to h); j) electric-field difference curves showing an abnormal p-n junction characteristic; there is no significant change in the potential from the cell bulk to the cell surface at the epoxy/Si interface; k–n) AFM and the corresponding KPFM of two types of normal/abnormal junction transition area (scale bar in c–n: $1\text{ }\mu\text{m}$).

junction if the local cell area is functioning normally. The appearance of the electric-field peak at the cell/epoxy interface suggests a significantly damaged junction; external reverse-bias voltage applied to the cell does not drop at the original position of the junction. In this case, because the Ag-epoxy/cell contact resistance should not be very small, the V_b drop at the interface—instead of at the junction—is consistent with a shunted junction if the equivalent resistance of the shunted junction is much smaller than the contact resistance at the epoxy/cell interface. Therefore, the abnormal electric potential/field is likely caused by junction damage or shunting.

Figure 1k–n show potential images in the transition region. We observed two types of transitions between the normal and abnormal junctions. The first is shown in Figure 1k and l, where the transition occurs in $\approx 1\text{ }\mu\text{m}$, which is about or slightly larger than the depletion range generated by a V_b of -1.5 V applied to the junction. This type has a relatively abrupt transition between the normal and damaged junctions. The second type is shown in Figure 1m and n, where the location of the electric-field peak is at a location significantly shallower than the normal junction depth. The green circle in Figure 1n indicates such an area adjacent to two junction-damaged areas. This apparent

movement of electric-field peak may be caused by a moderately damaged junction, an equivalent resistance of which is comparable to that at the epoxy/cell interface. The equivalent resistance depends on the quality of the junction, e.g., the gap state density and recombination velocity. In this case, V_b would drop at both the junction and interface. If the KPFM measurements cannot resolve the two voltage drops, then the electric-field peak would appear at a location between the junction and interface. Therefore, this type of transition may indicate a moderately damaged junction.

These rapid transitions associate with large areas of junction damage and suggest an actual material and junction degradation, rather than the well-reported local shunting induced by Na-decorated planar defects that penetrate p-n junction. One may argue that a high-density pinpoint shunt could also lead to the apparent junction collapse as the results shown in Figure 1h–j. If local shuntings were the reason for the observed large-area abnormal junction collapse, then the potential drop must gradually change from the abnormal area to the good area in over a much longer range of $\approx 100\ \mu\text{m}$, because the $\approx 100\ \Omega$ emitter sheet resistance would gradually increase resistance of the electrical current path through the local shunts and the emitter. However, the short transition distance indicates that the PID we observed should not be caused by local shunting; rather, it is likely dominated by actual large-area damage of material or junction. This is a new PID mechanism, and it has not been reported to date. Although reliable recombination current J_{02} could not be deduced from our dark I – V measurement, J_{02} was reported to increase with PID stressing,^[10,39] which is consistent with the large-area actual material and junction damages proposed here. Occurring probability of this type of PID should depend on the stressing conditions. Although we currently do not have a reliable statistic about the occurring probability, a significant portion of the PID was observed among the darkest areas of the cell stressed in the harsh conditions as described in the experimental section. Also, we worked on the Al-BSF cells from two c-Si cell manufactures, and this actual large-area material/junction degradation were all observed on the cells.

3.2. In situ KPFM Characterization

We developed in situ stressing capability in KPFM measurements^[33] to monitor the potential evolution across the p-n junction along with stressing voltage of $-1500\ \text{V}$ for more than 40 days (Figure 2). Initially, a fresh cell is confirmed in Figure 2a, e, and i, and the results are similar to the cell in Figure 1a–e. The potential difference amplitude is $\approx 1450\ \text{mV}$ between the emitter and the p-type bulk, consistent with the applied reverse-bias voltage of $-1.5\ \text{V}$. The electrical-field peak is $\approx 500\ \text{nm}$ to the Si/EVA interface, indicating a normal p-n junction (Figure 2e). After 20 days of PID stressing, the potential difference amplitude drops to $\approx 1000\ \text{mV}$ across the junction, and the electrical-field peak position shifts $\approx 200\ \text{nm}$ toward the Si front surface (Figure 2j). As the stressing continued for 40 days, the potential drop across the junction smears out, and there is no observable peak in the electrical-field curve (Figure 2k). After 300°C thermal annealing^[1,40] for 30 min, we observed a junction recovery similar to Figure 2f. The recovery is not fully healed back to a

normal junction when compared to Figure 2i. The potential difference increased to $\approx 1100\ \text{mV}$, and electrical-field peak position is similar to the 20-day stressed situation, suggesting a partial recovery. We also saw similar recovery after heat treatment in an ex situ lab-stressed sample as shown in Figure S3, Supporting Information.

Importantly, the potential evolution due to PID stress appears to be uniform over a long junction length. We note that Figure 2c, g, d, and h were combined by two image scans, and we scan a very large area of $\approx 350\text{-}\mu\text{m}$ total length along the junction with every image at $5 \times 5\ \mu\text{m}^2$. Over this long range, we consistently and uniformly observe the following: PID stressing makes the potential drop smaller and “junction” location shift to the front surface, and heat treatment partially recovers most of the area, except for some localized areas that are not recovered (Figure S4, Supporting Information). Our in situ results monitoring potential change across the junction validate above-mentioned ex situ KPFM data acquired from PID lab-stressed samples. And it is worth mentioning that the area underneath the metal grid can also be affected by heavy PID stressing; we observed similar degradation as Figure 2c, g, and k on the metal grid area of the 40-day stressed sample. It should be noted that, because no significant change was observed on the AFM image, the change in the V_b -induced potential drop across the junction during the in situ PID stressing should not be a result of surface contamination (e.g., Na migration onto the cross-sectional surface). Even if a thin Na-incorporated insulating layer below a few nm is formed during the PID, this thin contamination layer should not screen out the potential in the bulk, and the surface potential measurement should reflect the potential drop across the junction in the bulk.

3.3. Localized Current Collection

We performed EBIC imaging on similar pieces of fresh and heavily degraded areas as the KPFM measurements. Figure 3 shows that the EBIC images are very different between the fresh and degraded samples. Figure 3a shows an EBIC image taken on the fresh sample. The wide bright region ($\approx 10\ \mu\text{m}$) around the cell front face is consistent with a normal junction, which can collect current widely and operates as a regular solar cell. Note that surface recombination on the cross-section can also reduce the current collection depth, making a smaller apparent diffusion length from EBIC data. However, in a heavily degraded area (Figure 3b), the EBIC image shows much smaller current collection with a current intensity two orders of magnitude smaller than that of the normal junction. The EBIC contrast on the images was adjusted and is not related to the absolute magnitude of the EBIC current. This EBIC observation in the heavily degraded area is consistent with the KPFM potential imaging, where imaging for both the potential and current collection point to a malfunctioned junction, no potential barrier, no built-in field, and no minority carriers drifting through. Figure 3c shows a sharp transition area between the good and degraded junction (highlighted by the red circle); the degraded area has a much lower current collection, whereas the transition to the higher current collection area is abrupt within a few microns, which is consistent with the abrupt transition KPFM

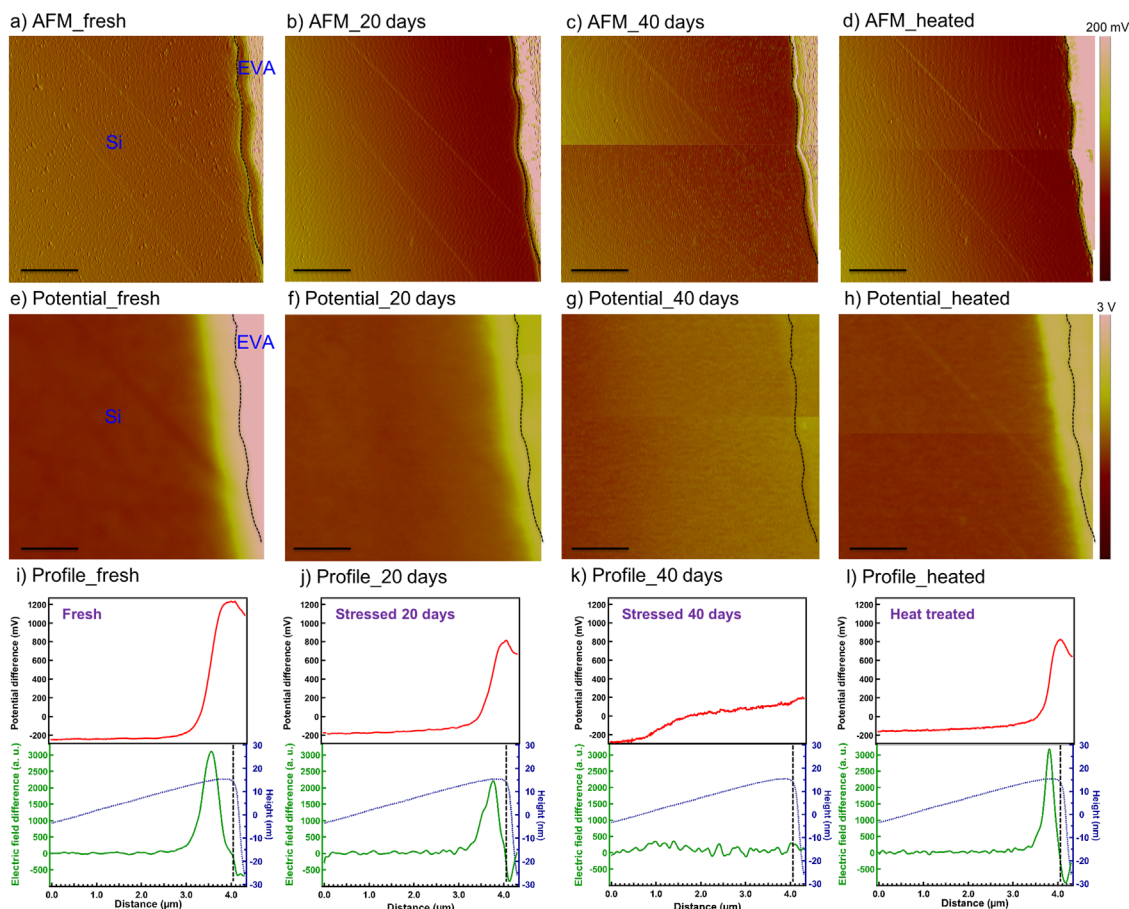


Figure 2. a–d) AFM images before *in-situ* PID stressing, after 20 days, 40 days, and heat-treated conditions, respectively; e–h) the corresponding KPFM image at -1.5 V; i–l) the corresponding potential profiles for the four conditions. During the PID stressing, the potential change amplitude at p-n junction decreases, and eventually smears out after 40 days. The electrical-field peak position moves from p-n junction to the Si/EVA interface after 20 days, and eventually to no observable peak. After heat treatment, the profiles partially recovered but were still not the same as the fresh one. The black dashed line indicates Si/EVA interface (scale bar: $1\ \mu\text{m}$).

results in Figures 1k–l. Figure 3d shows the line profiles of the good, transition, and degraded EBIC signal across the junction. Note that the EBIC contrast on the images was adjusted and is not related to the absolute magnitude of the EBIC current; also, the transition-area line profile was taken on the area between good and degraded areas.

3.4. Chemical and Electrical Imaging

Another piece that went through the same PID stress was studied by TOF-SIMS in plane view, with DLIT and EBIC results confirming the large degraded area. **Figure 4a** shows the optical image of the sample, and **Figure 4b** shows the thermal image

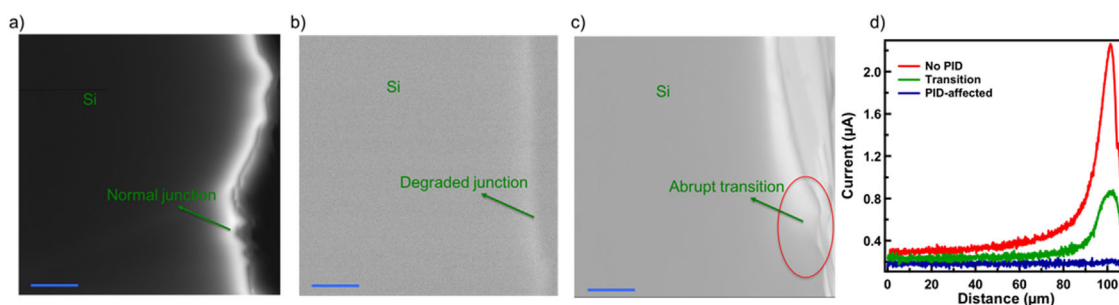


Figure 3. a) EBIC of current collection in normal junction area; b) PID-damaged area; c) transition area; d) current profiles across the p-n junction from the three areas. The EBIC contrast on the images was adjusted and is not related to the absolute magnitude of the EBIC current (scale bar: $20\ \mu\text{m}$).

(DLIT phase) taken at -1 V reverse bias modulated at 100 Hz. The DLIT image shows heat dissipation at several degraded locations, indicated as darker areas. Due to heat diffusion through the sample, the spatial resolution of the technique is relatively low, and we cannot determine whether the degraded areas are smeared point shunts or actual large-area degradation. We used EBIC to zoom into the area indicated by the purple rectangle. The result (Figure 4d) clearly shows a difference in EBIC current (bright in upper left and dark in lower right). In both the dark and bright regions, there are dark points that are probably induced by surface roughness. We highlight the sharp transition between dark and bright regions by overlaying the EBIC line profile (purple curve) along the orange line in Figure 4d. We note that the sharp change of dark and bright regions is not due to a mechanical defect such as a crack because no such defect can be identified by SEM (Figure 4c). The large dark region can be caused by poorer qualities of both/either the underlying Si material and/or junction—such as shorter minority-carrier lifetime (Shockley-Read-Hall (SRH) recombination) and larger diode quality factor (junction recombination)—than the brighter area. However, it cannot be caused by the effect of point shunts nearby because of the abrupt change of EBIC signal. If the EBIC bright/dark contrast resulted from a local shunting spot, then the EBIC current would gradually increase from the local shunting to defect-free areas. We also investigated the crystal orientation by EBSD, but there is no correlation between grain orientation and EBIC pattern (Figure S5, Supporting Information). We relate the abrupt change in the EBIC signal to the change in Na concentration from one area to the other due to the PID stress, as shown below. The reason for this difference in Na concentration and EBIC intensity between the two areas as well as the sharp transition boundaries between the areas requires further investigation.

We analyzed the EBIC-imaged areas by TOF-SIMS to investigate the chemical distribution of sodium. Figure 4e shows the 3-dimensional rendering of Na^+ over $500 \times 500 \mu\text{m}^2$. The Na^+ impurity map clearly correlates to the EBIC image. There are many needle-like features with localized high Na^+ concentration on the lower right region than the upper left region, which may be attributed to Na-decorated extended defects.^[13,14] In addition to the highly Na-containing local features, Na contamination concentrations are generally different in the dark and bright EBIC areas. In Figure 4f, we take the depth profiles in areas away from the localized highly Na-contaminated area but still in the regions with dark or bright EBIC signals. The red and blue points indicate the location for taking the Na^+ profiles. The dark-EBIC region has a Na^+ concentration of mid 10^{19}cm^{-3} , whereas Na is 2–5 times less in the bright-EBIC region. Also, we did TEM on a random area in the dark-EBIC region and found no extended defects in this region ($15 \mu\text{m}$ long, 100 nm wide, $15 \mu\text{m}$ deep) lifted out by FIB; results are shown in Figure S6, Supporting Information. Moreover, a cross-sectional sample was analyzed by TOF-SIMS, and considerably higher Na content was found in areas where the KPFM results showed a degraded junction, whereas lower or background-level Na profiles were observed in areas where KPFM results showed a normal p-n junction potential (Figure S7, Supporting Information).

To further study the impact of material lifetime in PID stressing, we applied μ -PCD to investigate the difference between unstressed and heavily PID-stressed silicon pieces. Prior to the measurement, we used hydrofluoric acid to etch off SiO_x and terminate the surfaces to ensure low surface recombination. PL imaging was performed to confirm that there are no visible localized defects on both samples (see Figure S8, Supporting Information). In Figure 4g, we show that the stressed sample has a faster initial carrier recombination rate at

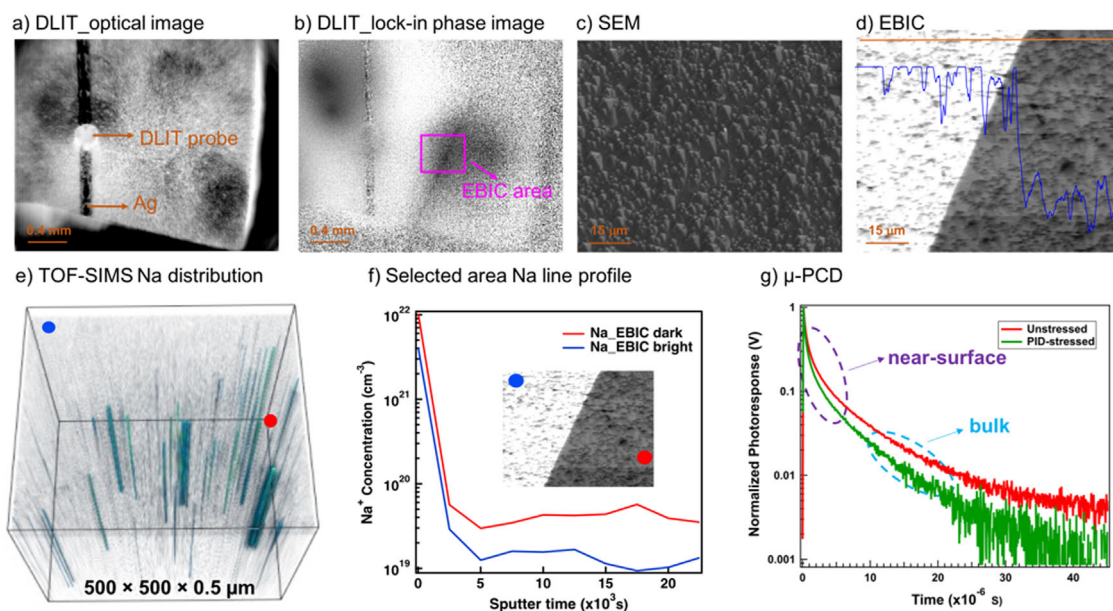


Figure 4. a) optical image of a stressed Si piece; b) DLIT phase image of the Si corresponding to a); c) SEM image of EBIC area; d) EBIC mapping of the pink rectangle area indicated in b); e) TOF-SIMS 3-D rendering of Na^+ ; f) Na depth profiles of EBIC dark and bright areas; inset is the EBIC image, and the red and blue spots indicate the location of Na profiles taken; g) μ -PCD lifetime measurement of fresh and stressed Si.

the fast time scale (0–5 μ s) when using a short-wavelength (500-nm) excitation with strong absorption at the top surface (\approx 1- μ m near-surface region). At later times (>10 μ s), we observe similar decay rates in both samples. These data suggest that the carrier lifetime is shorter near the surface for the stressed sample but similar in the bulk for both samples. The results show that PID stressing can cause silicon material degradation in the near-surface region. We also used transient reflection spectroscopy to probe the photogenerated charge-carrier dynamics close to the surfaces of the samples; we further confirmed faster decay of photogenerated charge carriers on the stressed sample (Figure S9 and Table S1, Supporting Information).

4. Discussion

Based on the characterization results above, we propose a new PID mechanism, different from and complementary to the commonly reported local shunting spots caused by Na-decorated extended defects (e.g., stacking faults). In addition to the localized regions of high Na concentration going into the depth of Si, the higher Na⁺ concentration in the dark-EBIC region suggests a higher concentration of point defects in the heavily PID-degraded area. Point defects formed by Na⁺ in Si have been reported to induce six gap states, two of which can be detrimental for photovoltaics, with one at 0.27 eV above the valence band maximum (VBM) (deep level) and the other being donor-like at 88 meV above the VBM.^[41] These two defects can, respectively, degrade the solar cell performance by different mechanisms of either SRH recombination or altering doping around the junction and in the Si bulk. More importantly, Na⁺ concentration in the PID area is high, on the order of up to 10^{19} cm⁻³ (for reference, the average Na⁺ concentration in Si bulk in ref. ^[41] is 10^{13} cm⁻³); so, the deep level can cause massive SRH recombination and massive lifetime degradation. If a p-n junction is formed by Si material with such a poor quality, then the junction cannot be well formed with leaky carrier transport through the gap states, causing a large reverse saturate current (J_0) and small equivalent resistance (R_j) of the junction. KPFM measures the voltage drop by measuring the potential change induced by applying a bias voltage to the device. If R_j is significantly smaller than the series resistance of other parts than the junction (including the electrical contacts and conduction lines), then the voltage drop will not be at the junction and KPFM shows no or a small voltage drop at the junction location. As for the effect on EBIC, if the lifetime of Si material is much degraded by SRH recombination, then minority carriers cannot be collected by the junction before they recombine, making a small EBIC current. On the other hand, the donor-like shallow state is just above the VBM, lower than all other acceptor-like states; so, this level with the high Na concentration can greatly alter the p-doping of Si on the order of $\approx 10^{16}$ cm⁻³—making the p-n doping boundary and the bulk p-doping nonuniform, and also making the doping of both n and p around the junction much smaller than the original p-n junction, and thus, widening the depletion region. This potential profile is consistent with the poor and irregular p-n interface with much lower carrier concentrations at both the p and n sides.

Table 1. Na ion (+1) charge diffusion barrier and estimated diffusion coefficient in Si with different strain rate (300 K).

Strain rate [%]	Barrier [eV]	D [cm ² s ⁻¹]
-0.05	1.253	2.73×10^{-24}
-0.03	1.260	2.12×10^{-24}
-0.01	1.168	7.43×10^{-23}
0.00	1.112	6.44×10^{-22}
0.01	1.052	6.31×10^{-21}
0.03	0.933	6.47×10^{-19}
0.05	0.815	6.02×10^{-17}

D_0 is estimated to be 3×10^{-3} cm² s⁻¹ using an average phonon frequency of 10^{13} Hz.

Models for why Na may penetrate certain areas as point defects and not others, and by what mechanism Na may be introduced into the Si bulk remain to be clarified. We performed a DFT calculation to estimate the diffusion coefficient of Na through stressed or strained silicon lattice. The results are shown in Table 1. The average phonon frequency was assumed to be a typical value in solids 10^{13} Hz.^[42] From these DFT results, the diffusion coefficient of Na in crystalline Si with 5% strain can be promoted by five orders of magnitude compared with stress/strain-free state at 300 K. This corresponds to a reduction of diffusion time of hopping to a neighboring lattice site from 10^5 to 4 s. Detailed mechanisms of the effect of Na and PID require further study.

5. Conclusions

We have proposed a new PID mechanism in conventional silicon modules that is essentially different from and complementary to the current knowledge that PID shunts are localized in small and separate spots. We found that degradation occurs not only at Na-decorated planar defects, but can also occur in large areas and can cause material and junction degradation. The KPFM potential and EBIC data elucidate consistent malfunctioned junction and deteriorated Si material with an actual large-area junction leakage, degraded lifetime, and shortened diffusion length—all of which can make the solar cell malfunction in the PID area. In situ KPFM results showed uniform potential evolution across the p-n junction; DLIT, EBIC, and TEM results are consistent with the large-area degradation. And TOF-SIMS illustrates that Na is also correlated to the PID in a large area. A large amount of Na can cause harmful point defects in Si. This study sheds new light on the c-Si PID mechanism, and it opens new paths to ultimately resolve PID, which is one of the most critical issues in photovoltaic module performance.

Supporting Information

Supporting information is available from the Wiley Online Library or from the author.

Acknowledgements

The authors thank Dr. Manuel Schnabel and Vincenzo LaSalvia (NREL) for hydrofluoric acid etching. C.X. thanks Dr. Harvey Guthrey (NREL) for EBIC training, and Prof. Yuanyue Liu (UTAustin) for fruitful discussion on theoretical calculation. This work was authored by the National Renewable Energy Laboratory, operated by Alliance for Sustainable Energy, LLC, for the U.S. Department of Energy (DOE) under Contract No. DE-AC36-08GO28308. Funding was provided by U.S. Department of Energy Office of Energy Efficiency and Renewable Energy Solar Energy Technologies Office under Agreement #30304. The views expressed in the article do not necessarily represent the views of the DOE or the U.S. Government. The U.S. Government retains and the publisher, by accepting the article for publication, acknowledges that the U.S. Government retains a nonexclusive, paid-up, irrevocable, worldwide license to publish or reproduce the published form of this work, or allow others to do so, for U.S. Government purposes.

Keywords

fundamental mechanisms, large-area damage, multiple characterization, potential-induced degradation, Si solar cells

Received: October 23, 2018

Revised: November 30, 2018

Published online:

- [1] S. Pingel, O. Frank, M. Winkler, S. Daryan, T. Geipel, H. Hoehne, J. Berghold, in *2010 35th IEEE Photovolt. Spec. Conf.*, **2010**, pp. 002817–002822.
- [2] P. Hacke, K. Terwilliger, S. Glick, D. Trudell, N. Bosco, S. Johnston, S. Kurtz, in *2010 35th IEEE Photovolt. Spec. Conf.*, **2010**, pp. 000244–000250.
- [3] E. Schneller, N. S. Shiradkar, N. G. Dhere, in *2014 IEEE 40th Photovolt. Spec. Conf. PVSC*, **2014**, pp. 3216–3219.
- [4] J. Berghold, S. Koch, S. Pingel, S. Janke, A. Ukar, P. Grunow, T. Shioda, *Reliab. Photovolt. Cells Modul. Compon. Syst. VIII. International Society For Optics And Photonics*, **2015**, p. 95630A.
- [5] W. Luo, Y. Sheng Khoo, P. Hacke, V. Naumann, D. Lausch, S. P. Harvey, J. Prakash Singh, J. Chai, Y. Wang, A. G. Aberle, S. Ramakrishna, *Energy Environ. Sci.* **2017**, *10*, 43.
- [6] J. Bauer, V. Naumann, S. Großer, C. Hagendorf, M. Schütze, O. Breitenstein, *Phys. Status Solidi RRL – Rapid Res. Lett.* **2012**, *6*, 331.
- [7] V. Naumann, D. Lausch, S. Großer, M. Werner, S. Swatek, C. Hagendorf, J. Bagdahn, *Energy Procedia* **2013**, *33*, 76.
- [8] V. Naumann, D. Lausch, A. Graff, M. Werner, S. Swatek, J. Bauer, A. Hähnel, O. Breitenstein, S. Großer, J. Bagdahn, C. Hagendorf, *Phys. Status Solidi RRL – Rapid Res. Lett.* **2013**, *7*, 315.
- [9] V. Naumann, D. Lausch, A. Hähnel, J. Bauer, O. Breitenstein, A. Graff, M. Werner, S. Swatek, S. Großer, J. Bagdahn, C. Hagendorf, *Sol. Energy Mater. Sol. Cells* **2014**, *120*, 383.
- [10] D. Lausch, V. Naumann, O. Breitenstein, J. Bauer, A. Graff, J. Bagdahn, C. Hagendorf, *IEEE J. Photovolt.* **2014**, *4*, 834.
- [11] B. Ziebarth, M. Mrovec, C. Elsässer, P. Gumbsch, *J. Appl. Phys.* **2014**, *116*, 093510.
- [12] V. Naumann, C. Brzuska, M. Werner, S. Großer, C. Hagendorf, *Energy Procedia* **2016**, *92*, 569.
- [13] S. P. Harvey, J. A. Aguiar, P. Hacke, H. Guthrey, S. Johnston, M. Al-Jassim, *IEEE J. Photovolt.* **2016**, *6*, 1440.
- [14] S. P. Harvey, J. Moseley, A. Norman, A. Stokes, B. Gorman, P. Hacke, S. Johnston, M. Al-Jassim, *Prog. Photovolt. Res. Appl.* **2018**, *26*, 377.
- [15] G. Xianfang, L. Xiaoyan, Y. Jingwen, W. Shaoliang, Z. Xin, Z. Su, F. Weitao, H. Qingsong, *Phys. Status Solidi A* **2017**, *214*, 1700006.
- [16] K. Wangemann, A. Metz, H. Nagel, *26th Eur. Photovolt. Sol. Energy Conf. Exhib.* **2011**, *4CO.5.6*, 3107.
- [17] P. Grunow, S. Krauter, S. Wendlandt, J. Berghold, D. Nieschalk, S. Koch, *27th Eur. Photovolt. Sol. Energy Conf. Exhib.* **2012**, *2CV.7.3*, 1985.
- [18] A. Masuda, A. Ogura, N. Ikeno, K. Hara, T. Doi, T. Yamazaki, T. Saruwatari, D. Imai, K. Ueno, A. Ogishi, K. Mishina, *28th Eur. Photovolt. Sol. Energy Conf. Exhib.* **2013**, *eBV.1.33*, 1139.
- [19] T. M. Kuan, C. C. Huang, L. G. Wu, Y. C. Chan, C. Y. Yu, *2013 IEEE 39th Photovolt. Spec. Conf. PVSC*, **2013**, pp. 2224–2226.
- [20] H. Antoniadis, J. Kapur, A. Meisel, D. Inns, J. Nee, H. Wang, X. Wang, R. Schulze, S. C. Pop, *31st Eur. Photovolt. Sol. Energy Conf. Exhib.* **2015**, *1AO.1.4*, 15.
- [21] X. Gou, X. Li, S. Zhou, S. Wang, W. Fan, Q. Huang, *Int. J. Photoenergy*, **2015**, *2015*, Article ID 863248.
- [22] W. Stein, S. Reichel, J. Höhne, E. Vetter, H. Schlemm, J. Mai, H.-P. Sperlich, B. Heinze, M. Runge, S. Frigge, M. Uhlig, U. Scheit, D. Decker, H. Mehlich, *27th Eur. Photovolt. Sol. Energy Conf. Exhib.* **2012**, *4VT.2.52*, 3411.
- [23] J. Li, Z. Qiu, C. Lu, Y. Li, Q. Jiang, X. Niu, W. Shan, W. Han, *28th Eur. Photovolt. Sol. Energy Conf. Exhib.* **2013**, *4AV.5.40*, 3309.
- [24] S. W. Glunz, M. Glatthaar, P. Saint-Cast, H. Nagel, *29th Eur. Photovolt. Sol. Energy Conf. Exhib.* **2014**, *5CO.14.5*, 2351.
- [25] J. Woods, I. Fidalgo, S. Ferrigan, C. Reid, *28th Eur. Photovolt. Sol. Energy Conf. Exhib.* **2013**, *4AV.5.49*, 3340.
- [26] I. Kueppenbender, B. Hamzavy, J. Norwood, A. Bennett, J. Kapur, *28th Eur. Photovolt. Sol. Energy Conf. Exhib.* **2013**, *1CV.2.10*, 476.
- [27] J. D. Lavandera Antolin, M. Cardinali, C. Liciotti, *29th Eur. Photovolt. Sol. Energy Conf. Exhib.* **2014**, *5BV.3.32*, 3093.
- [28] J. Berghold, S. Koch, B. Frohmann, P. Hacke, P. Grunow, in *2014 IEEE 40th Photovolt. Spec. Conf. PVSC*, **2014**, pp. 1987–1992.
- [29] J. Kapur, K. M. Stika, C. S. Westphal, J. L. Norwood, B. Hamzavtehrany, *IEEE J. Photovolt.* **2015**, *5*, 219.
- [30] “IEC TS 62804-1:2015 | IEC Webstore | rural electrification, solar power, LVDC,” can be found under <https://webstore.iec.ch/publication/23071>.
- [31] “The Performance of Photovoltaic (PV) Systems – 1st Edition,” can be found under <https://www.elsevier.com/books/the-performance-of-photovoltaic-pv-systems/pearsall/978-1-78242-336-2>.
- [32] D. C. Jordan, T. J. Silverman, J. H. Wohlgemuth, S. R. Kurtz, K. T. VanSant, *Prog. Photovolt. Res. Appl.* **2017**, *25*, 318.
- [33] C.-S. Jiang, M. Yang, Y. Zhou, B. To, S. U. Nanayakkara, J. M. Luther, W. Zhou, J. J. Berry, J. van de Lagemaat, N. P. Padture, K. Zhu, M. M. Al-Jassim, *Nat. Commun.* **2015**, *6*, 9397.
- [34] C. Xiao, C. Wang, W. Ke, B. P. Gorman, J. Ye, C.-S. Jiang, Y. Yan, M. M. Al-Jassim, *ACS Appl. Mater. Interfaces* **2017**, *9*, 38373.
- [35] C. Xiao, C.-S. Jiang, S. Johnston, X. Yang, J. Ye, B. Gorman, M. Al-Jassim, *Sol. Energy* **2017**, *158*, 746.
- [36] Z. Li, C. Xiao, Y. Yang, S. P. Harvey, D. Hoe Kim, J. A. Christians, M. Yang, P. Schulz, S. U. Nanayakkara, C.-S. Jiang, J. M. Luther, J. J. Berry, M. C. Beard, M. M. Al-Jassim, K. Zhu, *Energy Environ. Sci.* **2017**, *10*, 1234.
- [37] G. Kresse, D. Joubert, *Phys. Rev. B* **1999**, *59*, 1758.
- [38] J. P. Perdew, K. Burke, M. Ernzerhof, *Phys. Rev. Lett.* **1996**, *77*, 3865.
- [39] P. Hacke, R. Smith, K. Terwilliger, S. Glick, D. Jordan, S. Johnston, M. Kempe, S. Kurtz, *IEEE J. Photovolt.* **2013**, *3*, 246.
- [40] M. Winkler, B. Richardson, S. Pingel, H. Hoehne, O. Frank, J. Berghold, *25th Eur. Photovolt. Sol. Energy Conf. Exhib. 5th World Conf. Photovolt. Energy Convers. 6-10 Sept. 2010 Valencia Spain* **2010**, 3753.
- [41] E. H. Dahl, J. Madsbøll, A.-K. Søiland, J.-O. Odden, R. Tronstad, A. N. Larsen, *Semicond. Sci. Technol.* **2013**, *28*, 105010.
- [42] R. Hull, *Properties of Crystalline Silicon. The Institution of Electrical Engineers, London, United Kingdom* **1999**.
- [43] M. M. Waegle, X. Chen, D. M. Herlihy, T. Cuk, *J. Am. Chem. Soc.* **2014**, *136*, 10632.
- [44] X. Chen, S. N. Choing, D. J. Aschaffenburg, C. D. Pemmaraju, D. Prendergast, T. Cuk, *J. Am. Chem. Soc.* **2017**, *139*, 1830.